Journal of Materials Research and Technology 39 (2025) 7453–7468

Contents lists available at ScienceDirect

Journal of Materials Research and Technology

journal homepage: www.elsevier.com/locate/jmrt

Tribocorrosion performance of additively manufactured CuNi30 and SS-316L in marine environment: Seawater resistant alloys

Muhammad Ammar Anjum [a,*], Ananya Nath [d], Sneha Goel [b], Ermei Mäkilä [c], Sagar Sarkar [d], Antti Salminen [a], Ashish Ganvir [a]

[a] Department of Mechanical and Materials Engineering, University of Turku, Turku, Finland
[b] Advanced Materials for Nuclear Energy, VTT Technical Research Centre of Finland, Finland
[c] Department of Physics and Astronomy, University of Turku, Turku, Finland
[d] Department of Mechanical Engineering, Indian Institute of Technology Delhi, India

A B S T R A C T

This study presents the first systematic investigation of the tribocorrosion resistance of additively manufactured CuNi30 in artificial seawater (ASTM D1141-98), along with mechanical and tribocorrosion performance comparison against SS-316L. Both alloys were produced by laser powder bed fusion (PBF-LB/M), achieving relative densities of 99.8 % (CuNi30) and 99.1 % (SS-316L). The as-built CuNi30 exhibited a tensile strength of 503 MPa, which increased to 638 MPa after heat treatment at 550 °C for 2 h, reaching parity with SS-316L. Phase identification through X-ray diffraction confirmed the precipitation of Nb-rich precipitates ($NbNi_3$) after heat treatment which contributed to the observed strengthening. The tribocorrosion performance was evaluated using a ball-on-disk setup, where potentiostatic, potentiodynamic, EIS, and COF measurements were recorded under both static and sliding conditions to assess corrosion-wear interactions. The results revelated that SS-316L is more susceptible to tribocorrosion damage due to its lower polarization stability and the formation of thin unstable third body layer. The calculated wear rate showed a decrease from 9.07 × 10^{-8} mm^3/N·mm for SS-316L to 2.08 × 10^{-8} mm^3/N·mm for heat-treated CuNi30, highlighting the superior tribocorrosion resistance of CuNi30.

1. Introduction

The advancement of the marine industry has led to an increased emphasis on the development of new materials designed to withstand the challenging marine conditions. Marine materials face challenges due to the high salinity, prevalent biofouling, and unstable pH in seawater that leads to corrosion assisted mechanical failure [1]. Austenitic stainless-steel grades are used in critical marine components such as marine fittings, pumps, valves, propeller shafts and structural elements to withstand the severe marine conditions due to adequate corrosion resistance and ease of maintenance. However, their poor biofouling and wear resistance necessitates frequent maintenance and replacement which consequently leads to high operational costs [2].

Copper-nickel alloys, such as CuNi10 and CuNi30, have emerged as promising alternatives to stainless steels in seawater piping, condenser tubes, bearings, and valves due to their exceptional biofouling resistance and superior seawater corrosion resistance [3,4]. The superior corrosion resistance of CuNi30 alloys is primarily attributed to the development of a strong self-repairing oxide film of Cu_2O where Ni helps reduce the defect density in the oxide layer by occupying the cation vacancies, enhancing long-term stability [5,6]. To make the mechanical properties of CuNi30 at par with SS-316L, niobium addition is commonly employed. Niobium improves the tensile behaviour through grain refinement and precipitation hardening. It has been reported that 1 % niobium addition in CuNi30 enhances its mechanical strength through NbC triggered grain refinement and nano-precipitates dislocation interaction via. Orowan bypassing [7].

Conventional manufacturing of copper-nickel alloys is mainly based on continuous casting, which suffers from long production cycles, limited design flexibility for customization, and inherent casting defects [8]. The slow solidification associated with conventional casting, leads to the rejection of Ni rich solutes from the solid into the solidifying liquid causing compositional inhomogeneities such as coring and micro segregation [9,10]. These defects negatively impact mechanical performance and corrosion resistance of casted parts. Hence there is a clear need for alternative processing techniques that enable finer microstructures, improved mechanical properties, and enhanced corrosion resistance. Studies have demonstrated that increasing the solidification rate homogenizes the microstructure and reduces the elemental segregation in metal alloys thus potentially solving these problems. Hence

* Corresponding author.
E-mail address: muaanj@utu.fi (M.A. Anjum).

https://doi.org/10.1016/j.jmrt.2025.10.247
Received 7 August 2025; Received in revised form 29 October 2025; Accepted 29 October 2025
Available online 30 October 2025

Table 1
Chemical composition of CuNi30 and SS-316L alloy powders used in this study.

Material	Chemical Composition										
CuNi30	**Element**	**Cu**	**Ni**	**Fe**	**Mn**	**Nb**	**Si**	**C**	**S**	**P**	**Pb**
	wt%	Bal.	30.3	1.0	1.0	0.9	0.4	0.002	0.002	0.01	0.002
SS-316L	**Element**	**Fe**	**Ni**	**Cr**	**Mn**	**Mo**	**Si**	**C**	**S**	**N**	**P**
	wt%	Bal.	12.5	17.8	0.9	2.4	0.64	0.02	0.01	0.1	0.007

laser based additive manufacturing techniques such as laser-direct energy deposition (L-DED) and laser powder bed fusion (PBF-LB/M), can address these limitations by enabling localized melting, rapid solidification, and layer-by-layer fabrication, resulting in fine-grain microstructures, minimal elemental segregation, and superior mechanical performance [11–14]. Additive manufacturing processes eliminate the need for traditional moulds and tooling, offering high design flexibility for complex, lightweight marine structures such as hollow thruster blades, valves, and cooling system components.

The laser based additive processing of copper alloys is quite challenging due to the low infrared laser beam absorption of copper, which affects sable melt pool formation and consolidation. To overcome this, strategies such as alloying and surface powder modification have been employed, facilitating successful PBF-LB/M processing of a range of copper-based alloys, including Cu–Cr, Cu–Al, and Cu–Ni systems [15–18]. Among these, cupronickel alloys have gained attention for high-performance, custom-engineered marine components. While the mechanical performance and electrochemical characterization of conventionally manufacture cupronickel alloys are well documented, studied on the AM counterparts are limited. Nadimi et al. [19] investigated the corrosion and microstructural properties of PBF-LB/M processed CuNi30 (C96400) alloy and reported elongated grain formation in PBF-LB/M processed part along with slight improvement in corrosion resistance. In another work Liu et al. [20] compared the mechanical properties and corrosion resistance of PBF-LB/M processed CuNi30 with wrought counterpart. The results showed a substantial decrease in average grain size due to the formation of refined sub-grain structure along with increased dislocation density as a result of rapid solidification which led to improved tensile properties. Additionally, PBF-LB/M processed CuNi30 showed improved corrosion resistance which was linked to heterogenous passive film formation. In order to examine the effect of printing orientation on microstructure and mechanical performance, Roshan et al. [21] investigated PBF-LM/M processed CuNi30 samples and reported that vertically build samples showed 13 % (from 426 MPa to 370 MPa) and 9 % (521 MPa–470 MPa) decrease in yield and tensile strength respectively along with improved ductility of 19 %.

Apart from mechanical strength and corrosion resistance, tribocorrosion (the simultaneous interaction of wear and corrosion) is the leading cause of material degradation in marine environments. The combined influence of mechanical damage and electrochemical degradation makes tribocorrosion a highly complex and severely destructive process [22,23]. In marine applications, seawater pumps, rudders, bearings, valve bodies, impellers, and sleeves experience tribocorrosion degradation [24,25]. The failure vulnerability of these components can lead to the collapse of entire marine equipment, resulting in major safety risk [26,27]. Although over the past two decades, Additive Manufacturing has been widely adopted in aerospace and automotive industries, yet its acceptance in marine applications remains limited due to the unexplored corrosion, corrosion fatigue and tribocorrosion performance of additively manufactured (AMed) metal alloys. While several studies have explored the tribocorrosion resistance of conventionally manufactured SS-316L and CuNi30 [28–30], no prior research has systematically investigated the tribocorrosion behaviour of AMed CuNi30 and compared it with tribocorrosion resistance of AMed SS-316L. In a recent study, Stachowiak, A. et al. demonstrated that PBF-LB/Inconel718 exhibited higher tribocorrosion resistance than its cast counterpart due to fine microstructure and compact oxide layer formation [31]. This suggests that PBF-LB/M processed CuNi30 and SS-316L could possess high tribocorrosion resistance, but this remains unexplored.

This study presents the first systematic investigation of the tribocorrosion resistance of AMed CuNi30 and compares its performance with AMed SS-316L in a simulated seawater environment. Both alloys were fabricated using PBF-LB/M technique, followed by mechanical property evaluation and tribocorrosion characterization. Additionally, heat treatment was optimized for CuNi30 alloy to enhance its mechanical performance. By bridging the knowledge gap on the tribocorrosion behaviour of additively manufactured CuNi30, this work lays the foundation for expanding its use in marine components, offering a more durable and cost-effective alternative to SS-316L.

2. Materials and method

2.1. Material and PBF-LB/M processing

The CuNi30 alloy powder used in this study was obtained from Electro-Optic Systems (EOS) GmbH. EOS CuNi30 is a copper-nickel alloy that has excellent corrosion resistance in seawater. The material complies with ASTM B369-09 standard and UNS 96400 specifications [32]. This gas-atomized powder was specifically designed for the PBF-LB/M process. The elemental composition of the CuNi30 powder batch measured using optical emission spectrometer as provided by the manufacturer is detailed in Table 1.

The morphology of the CuNi30 powder was analysed using Thermo Scientific Apreo scanning electron microscope (SEM). The SEM micrograph, as shown in Fig. 1, reveals predominantly spherical particles with

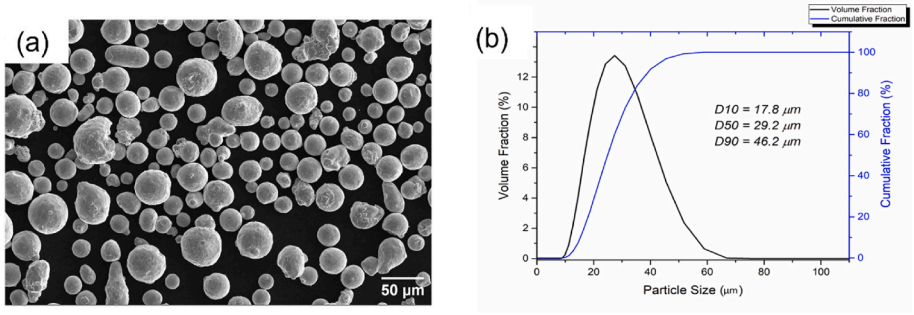

Fig. 1. Properties of CuNi30 powder used in this study (a) SEM image of powder morphology and (b) particles size distribution measured using laser diffraction.

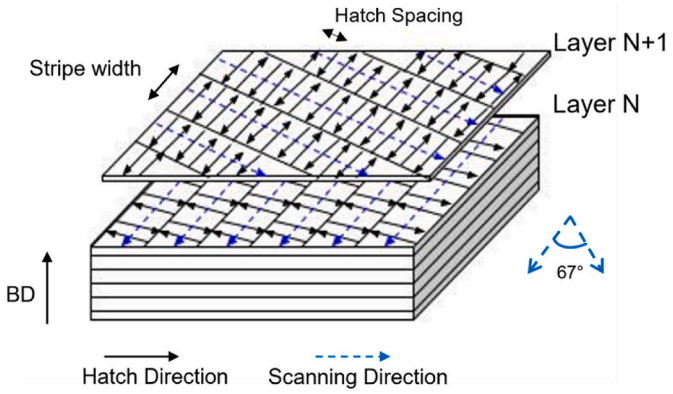

Fig. 2. Schematic of the stripe hatching pattern used for the PBF-LB/M processing of CuNi30 and SS-316L alloy powders.

minimal satellite formation, indicative of high-quality gas-atomized powder. This morphology ensures optimal flowability and packing density, both critical for the PBF-LB/M processing.

The particle size distribution (PSD) of the CuNi30 powder was determined using a laser diffraction particle size analyser, Malvern MS3000. The PSD curve shown in Fig. 1 (b) indicates that the powder size distribution is within the range of 8.7–66.9 μm, which is ideal for PBF-LB/M, as it ensures a balance between layer thickness and laser absorption efficiency. For SS-316L, the powder was procured from Nikon SLM Solutions Group AG. The composition of the SS-316L powder batch is listed in Table 1. This material complies with ASTM A276 and DIN EN 10088 standards [33]. The powder morphology and PSD of this powder has already been reported by authors in earlier work [34].

Aconity MIDI + machine was used to fabricate the AM specimens. The system has a single-mode fiber laser with a maximum power of 400W. In the Aconity material database processing parameters of CuNi30 are not listed, so in order to optimize the parameters, a design of experiment (DOE) approach was adopted utilizing the response surface methodology (RSM). Details of DOE are given in the appendix. The laser beam diameter of 0.08 mm and powder layer thickness of 0.03 mm were kept constant throughout the experiments. The oxygen level of <100 ppm was maintained throughout the processing. A strip hatching pattern was used for laser scanning with 67° rotation between each layer. The schematic of the laser scanning strategy is provided in Fig. 2.

A total of 16 samples were made for process parameter optimization. The relative density of each sample, determined using Archimedes' principle, along with the upskin surface roughness, were measured afterwards. The optimized parameters for CuNi30 alloy were selected based on the maximum achieved density value and are listed in Table 2. For each sample, the density was measured five times, and the surface roughness was measured three times, and the respective average values have been reported. For SS-316L the optimized parameters of laser power, scan speed, and hatch spacing listed on Aconity material database were selected, which are given in Table 2 along with the achieved density and roughness values. Additionally, microscopic image-based quantification was performed to complement the Archimedes measurements. The average porosity, pore circularity and pore size distribution are summarized in Table 2.

2.2. Material characterization

X-ray diffraction analysis was performed using Malvern Panalytical Aeris equipment with Cu-Kα radiation. The 2θ range was selected from 20° to 90°. For microstructural characterization, the as-built and heat-treated samples were fine-ground down to Struers 4000 abrasive paper, followed by final polishing with 1 μm diamond suspension on an MD-Nap cloth to achieve a mirror-like surface finish using Struers LaboForce 100 grinding/polishing machine. Motic AE2000 MET inverted microscope was used for optical imaging, whereas for SEM images and EDS elemental mapping, Thermofisher Apreo equipped with Oxford instruments UltimMax 100 EDS detector was used.

2.3. Heat treatment and mechanical testing

Heat treatment of as-built CuNi30 samples was carried out to further enhance the tensile strength. Three different heat treatment cycles were studied to identify the most optimal heat treatment procedure. The samples were heated under ambient conditions with a constant holding time of 120 min at three distinct temperatures: 550 °C, 600 °C, and 650 °C, followed by air cooling. To compare the influence of each heat treatment operation, Vickers hardness testing (HV2.5) of the samples was performed using Falcon 608 microhardness tester. For tensile testing, a 120 × 30 × 15 mm (Length x width x height) block was built using PBF-LB/M. The tensile specimens were machined using an EDM wire-cutting machine (Charmilles Roboform 55). ASTM E8 [35] sub-size specimen dimensions were followed for the machining of dog-bone specimens, as shown in Fig. 3. Three specimens were tested for each material. All the tensile tests were conducted with a constant strain rate of 0.003/s at room temperature.

Table 2
PBF-LB/M optimized process parameters, along with the measured relative density and surface roughness values.

Material	Process Parameters	Relative density (%) Archimedes	Relative density (%) Image Analysis	Mean Pore Size (μm^2)	Circularity	Up-skin surface roughness Sa (μm)
CuNi30	*Laser power* 300W *Scan speed* 1000 mm/s *Hatch spacing* 0.08 mm	99.71 ± 0.05	99.92 ± 0.10	117.8 ± 78.5	0.34 ± 0.07	5.4 ± 0.2
SS-316L	*Laser power* 150W *Scan speed* 900 mm/s *Hatch spacing* 0.08 mm	99.13 ± 0.14	99.44 ± 0.27	207.2 ± 98.4	0.30 ± 0.03	7.2 ± 0.4

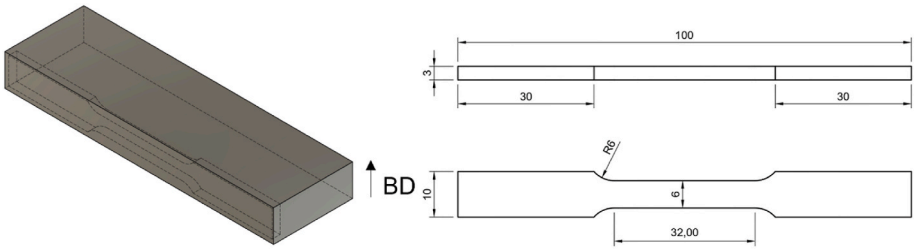

Fig. 3. Configuration of tensile specimen and the specimen size as per ASTM E8. The built direction (BD) is indicated by the arrow.

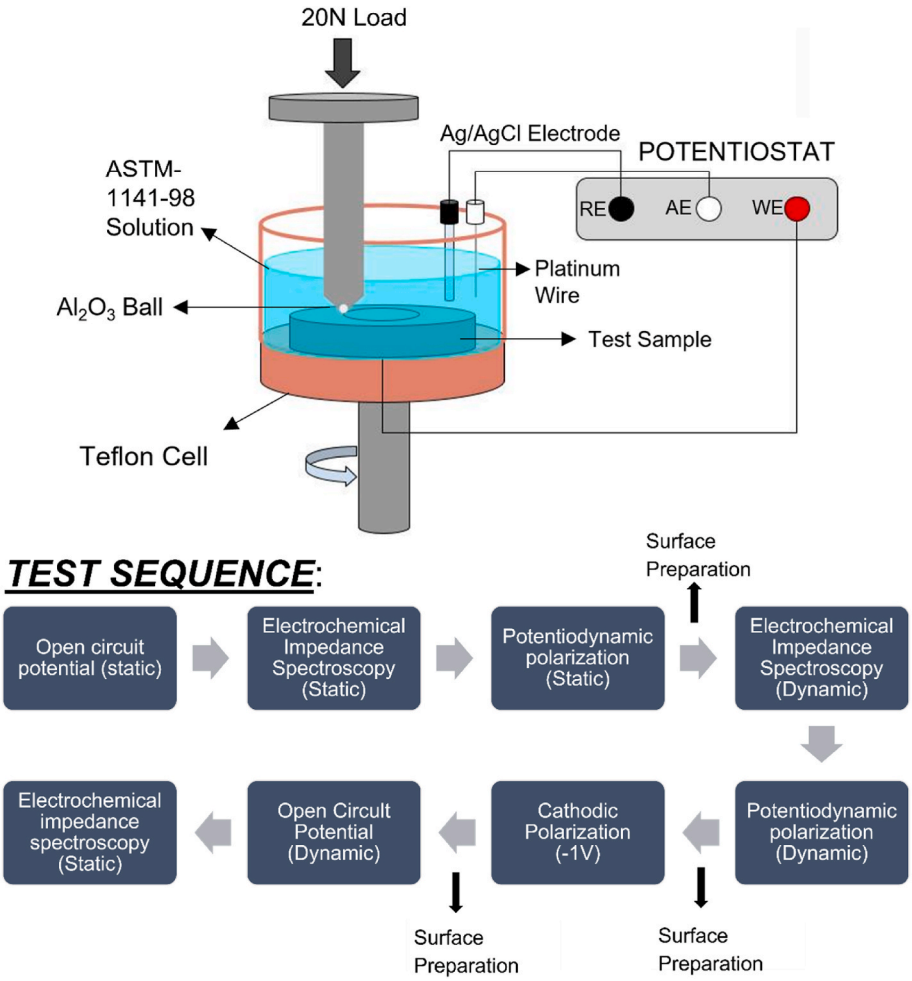

Fig. 4. Schematic of the experimental setup designed for the tribocorrosion testing and the test sequence adopted for the tribocorrosion experiments.

2.4. Tribocorrosion testing

For tribocorrosion testing, a ball-on-disk method was employed in conjunction with potentiostat to measure the potential change using three electrode method. Tribocorrosion experiments were performed on Ducom POD-4.0 tribometer integrated with Ivium vertex potentiostat. Disc-shaped specimen with dimensions of 60 mm in diameter and 7 mm in thickness were used. Before starting the test, the samples were ground and polished down to 0.25 μm surface roughness. The working electrode was connected to the sample from the base, with a platinum wire used as the counter electrode, and Ag/AgCl as the reference electrode filled with KCl electrolyte (36 % w/w). An Al_2O_3 ball of 6 mm diameter was used as the counter surface. A schematic diagram of the test setup is provided in Fig. 4 along with the test sequence. Both materials were tested at -1V cathodic (pure mechanical wear) and open-circuit potential (tribo-corrosion conditions). Before starting the potential measurement, the system was stabilized for 30 min. Static open circuit potential (OCP) was measured for 10min before starting the ball-on-disk wear test. Afterwards, the tribocorrosion test was run for 60min followed by OCP monitoring for another 10min without friction. A circular pattern was used to make the wear track. All tests were conducted at a constant friction speed of 30 mm/s and friction load of 20 N. For electrochemical impedance spectroscopy (EIS) the signal amplitude was 10 mV and the selected frequency range was from 0.01Hz to 100 KHz.

In order to simulate the seawater environment, an artificial seawater solution was made according to ASTM D1141-98 standard excluding heavy metal as per standard provision [36]. It has been reported that the solution specified in the ASTM D1141-98 standard better mimics the seawater environment compared to commonly used 3.5 % NaCl solution where the corrosion rate can be 4 higher than in the natural seawater [37]. The chemical composition of synthetic seawater used in this study is given in Table 3. To adjust the pH of solution a 0.1 M NaOH solution was used. All the tests were performed at a pH value of 8.01 and at room temperature 23 °C. Temperature and pH values were calculated before and after tribocorrosion test which showed a small increase in pH value (8.09 for CuNi30 and 8.17 for SS-316L), however temperature of the solution showed no significant difference.

3. Results & discussion

3.1. Microstructure characterization

XRD patterns of CuNi30 powder and the corresponding PBF-LB/M processed specimen along the building direction is provided in Fig. 5.

Table 3
Chemical composition of the simulated sea water solution used as per ASTM D1141-98.

Compound	NaCl	$MgCl_2$	Na_2SO_4	$CaCl_2$	KCl	$NaHCO_3$	KBr	H_3BO_3	$SrCl_2$	NaF
Concentration (g/L)	24.53	5.20	4.09	1.16	0.695	0.201	0.101	0.027	0.025	0.003

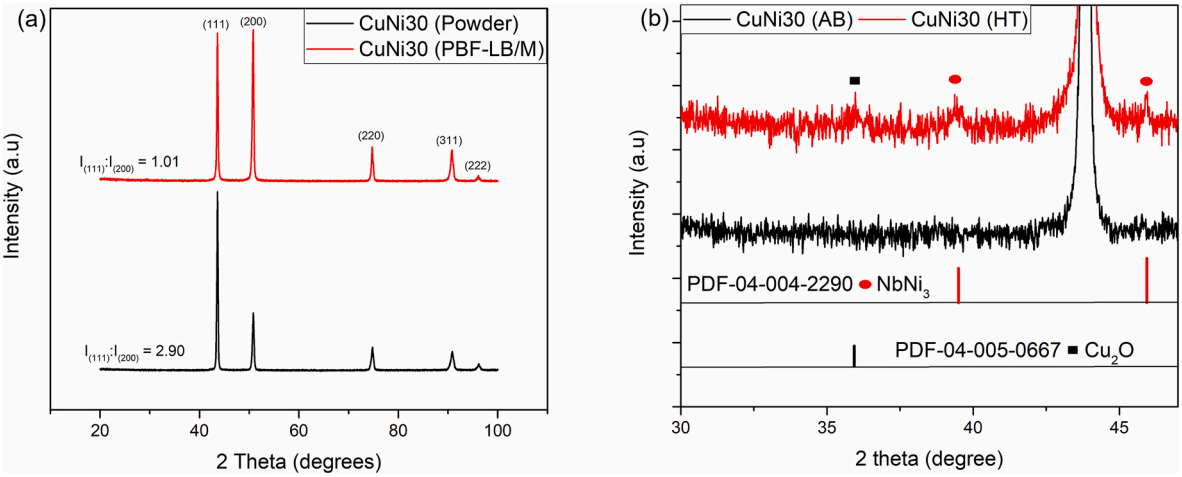

Fig. 5. (a)XRD pattern of CuNi30 powder and PBF-LB/M processed part showing high texture in case of PBF-LB/M processed part (b) XRD pattern for CuNi30 in as-built and heat-treated condition showing the precipitation of Nb rich precipitates after heat treatment.

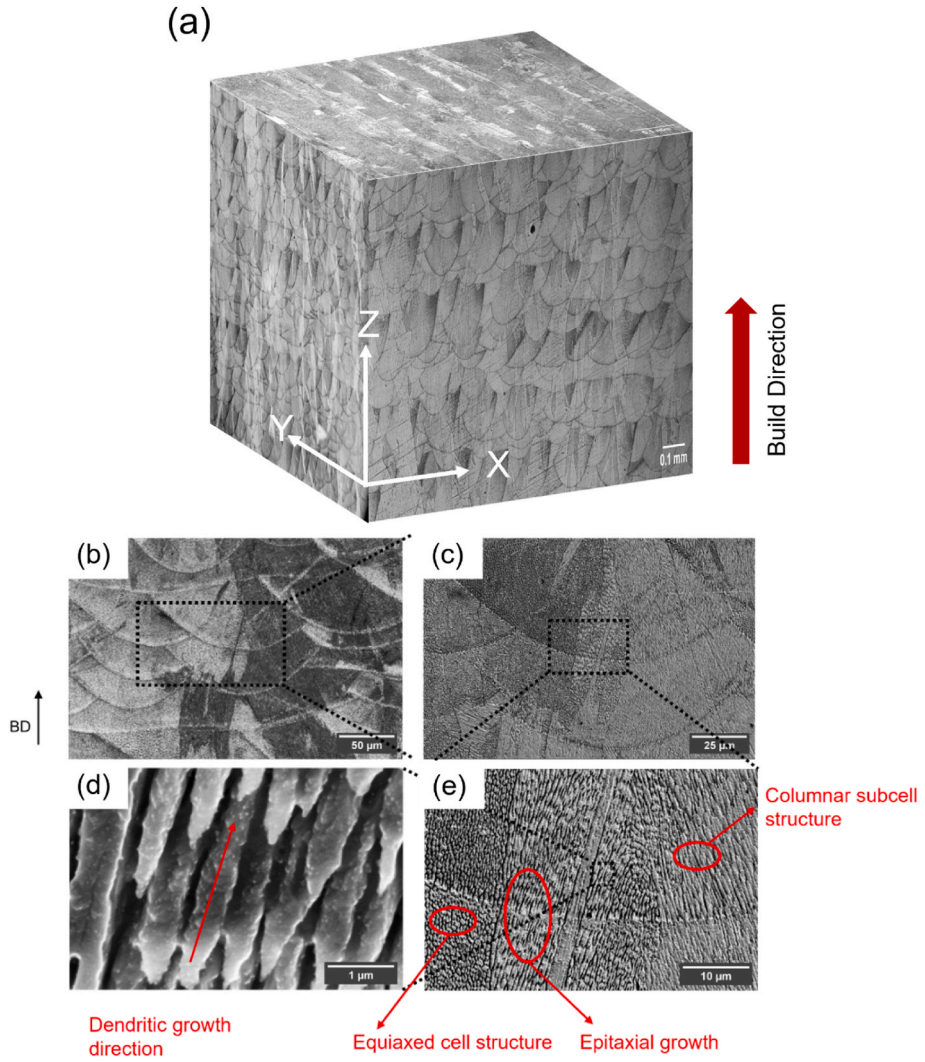

Fig. 6. (a) 3D optical view of CuNi30 samples showing melt pool boundaries and columnar grain growth (b–e) SEM images at different magnifications revealing equiaxed and columnar substructure and dendritic growth.

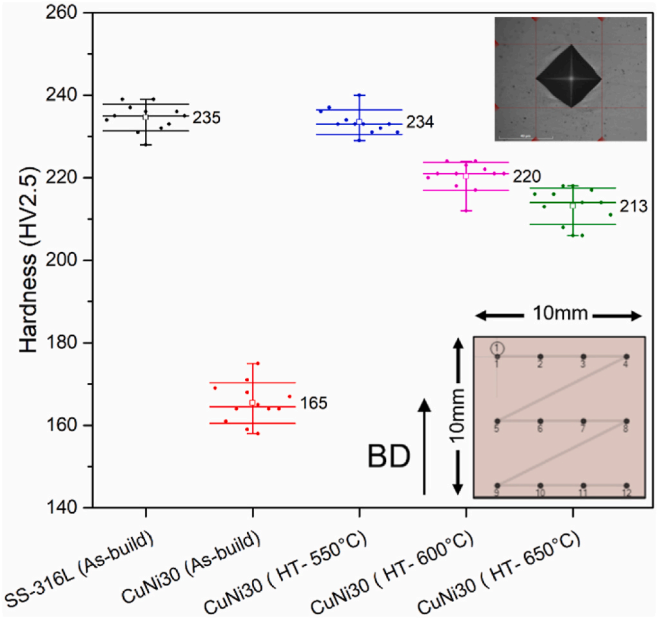

Fig. 7. Vickers microhardness of PBF-LB/M processed SS-316L and CuNi30 alloy in as-built and heat-treated condition.

The results show a single-phase bimetallic FCC structure in both cases. Peaks were observed at 2θ values of 43.66°, 50.86°, 74.86°, 90.94° and 96.14° that indicates a distorted FCC lattice structure relative to pure copper FCC lattice due to the incorporation of Ni atoms. In comparison with the powder sample, the PBF-LB/M processed sample showed a higher (200) peak that indicates preferential orientation along <100> direction due to the presence of larger thermal gradient along the building direction [20,38]. In order to identify the precipitate formation in as-built and subsequently heat-treated samples a slow XRD scan was carried out in the 2θ range of 30–47°. A multi-scan averaging method was used to reduce signal to noise ratio in the XRD data. The slow scan revelated the presence of $NbNi_3$ precipitate peaks at 2θ angle of 39.2° and 45.8° after heat treatment, consistent with reported literature on the formation of Nb rich precipitates after heat treatment in PBF-LB/M processed CuNi30 alloy [21].

Optical micrographs of PBF-LB/M processed CuNi30 are presented in a 3D prespective in Fig. 6. The melt-pool morphology and laser tracks are visible in the front and top view of Fig. 6(a). The micrographs show typical PBF-LB/M processing characteristic with overlapping melting tracks and layered microstructure with ripple pattern [39]. In PBF-LB/M, the melt pool dimensions are influenced by the input process parameters, and the discontinuities observed between successive melt pool tracks are caused by the laser scan strategy which involves 67° rotation for each additional layer [40].

SEM micrograph of the cross-section view along the building direction is presented in Fig. 6(b–e) showing both melt pool boundaries and internal grain morphology. Fig. 6(b) shows elongated grains preferentially oriented along the building direction extending across multiple melt pools. Within these grain as shown in Fig. 6(c) sub-grain structure is observed—an array of narrow, elongated sub-grains exhibiting either columnar or equiaxed morphology. The morphology of the subgrain structure (equiaxed and columnar) is linked to the complex non-equilibrium thermal history, rapid cooling rate, and a variation in chemical composition resulting from the slow homogenization kinetics of larger atoms as reported by several researchers [41,42].

3.2. Mechanical behaviour

3.2.1. Microhardness

Macro indentation hardness was performed on as build SS-316L and CuNi30 samples along with heat treated CuNi30 samples which were heat treated at three different temperatures i.e., 550 °C, 600 °C and 650 °C to optimized heat treatment process. The hardness results are plotted in Fig. 7. The graph shows that for CuNi30 the maximum hardness of 234HV was achieved when heat treatment was performed at 550 °C for 2 h which is comparable to the SS-316L as-built hardness value of 235HV. The reason for hardness increase is likely the precipitation of Nb rich precipitates as observed in the XRD results consistent with the previous studies conducted on similar metal alloys [21,43–45]. Roshan et al. reported that the increase in strength of CuNi30 following heat treatment is attributed to reduced solute segregation, stabilization of dislocation substructures, and possible precipitation hardening [21]. With further increase in heat treatment temperature a slight decrease in hardness was observed likely due to over-aging, since faster diffusion rates cause precipitates to coarsen quickly reducing their number density and increasing the inter-particle spacing [45].

Table 4
Average tensile properties of PBF-LB/M processed CuNi30 (as-built and HT 550 °C) and SS316L (as-built) alloys.

Material	Yield strength ($\sigma_{0.2}$, MPa)	Tensile strength (σ_{UTS}, MPa)	% Elongation
CuNi30 (AB)	418 ± 17	503 ± 23	29.6 ± 4.7
CuNi30 (HT)	517 ± 9	638 ± 8	24.5 ± 9.1
SS-316L	591 ± 12	662 ± 21	23.1 ± 3.6

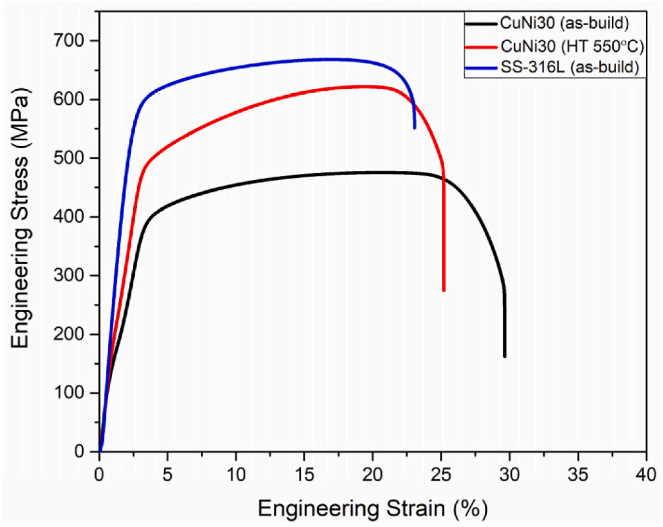

Fig. 8. Engineering stress-strain curves for CuNi30 (as-built and after HT 550 °C) and SS-316L samples.

3.2.2. Tensile properties

The heat treatment condition that resulted in maximum hardness was selected for further tensile testing, i.e., 550 °C for 2h. The tensile properties of CuNi30 (as-built), CuNi30 (heat treated at 550 °C, referred as HT) and SS-316L (as-built) samples are listed in Table 4. The representative tensile stress-strain curves for all three materials are presented in Fig. 8. All samples showed the existence of necking, indicating plastic deformation before fracture (see Fig. 9).

Both as-built and heat treated CuNi30 samples exhibited lower yield and tensile strengths compared to as-built SS-316L material. For CuNi30, post process heat treatment resulted in 24 % increase in yield strength at the expense of 17 % reduction in elongation. Overall, the heat-treated CuNi30 samples demonstrated tensile properties that closely approached those of the as-built SS-316L.

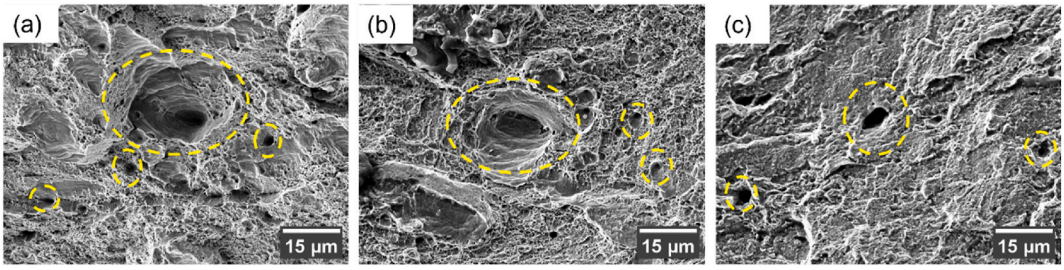

Fig. 9. Fracture micromorphology of (a) CuNi30(AB), (b) CuNi30(HT), and (c) SS-316L tensile specimens presenting micron size dimples which indicates ductile fracture characteristics.

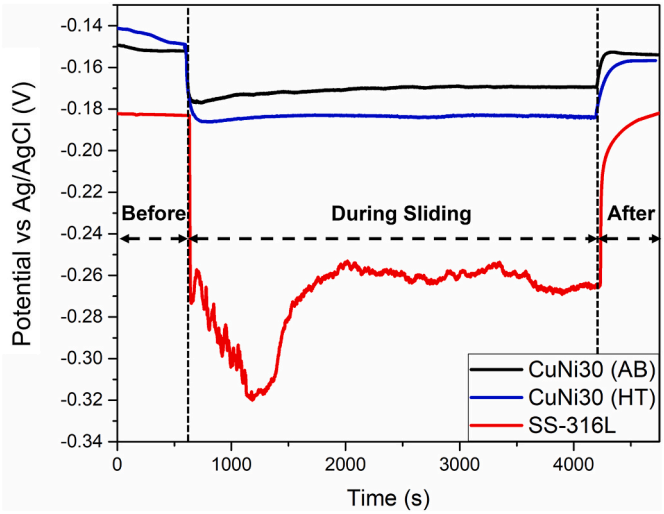

Fig. 10. Open Circuit Potential curves for CuNi30 (AB & HT) and SS-316L, with and without sliding wear, indicating the decrease in potential due to sliding wear.

The fracture surfaces of all tensile specimens were further investigated in detail using SEM. The fracture surface of all samples showed typical ductile fracture characteristics where micron sized dimples formation suggests sufficient plastic deformation. In fractography, the dimple size and morphology is related to material's ability to deform plastically with larger and deep dimples correspond to higher ductility [46–48]. The equiaxed shaped deep dimples in case of CuNi30(as-built) sample indicate sufficient plastic deformation consistent with the tensile test results (refer Table 4). In contrast, the SS-316L sample which exhibited lowest % elongation, showed finer dimples and regions with quasi-cleavage morphology indicating limited ductile deformation.

3.3. Tribocorrosion analysis

3.3.1. Electrochemical results

Mechanical friction can significantly accelerate electrochemical reaction by constantly disrupting passive film, exposing reactive metal surface. Hence the monitoring of OCP under static and sliding conditions provide valuable information about the change in electrochemical state of material surface. Fig. 10 shows the evolution of OCP for CuNi30(AB), CuNi30(HT) and SS-316L samples during tribocorrosion experiment. Before the start of sliding wear, a stable corrosion state with an OCP of −0.152V, −0.150V and −0.182V was observed for CuNi30(AB), CuNi30 (HT) and SS-316L, respectively. At the onset of friction, the OCP dropped sharply to a more cathodic potential due to tribocorrosion activation. With continued sliding, the OCP gradually stabilized to a steady state, indicating the establishment of a dynamic equilibrium between mechanical depassivation and electrochemical repassivation. For CuNi30, this equilibrium was established quickly, whereas SS316L took more time to come to a stable state. This can be ascribed to the passive layer characteristics and surface properties of material. Additionally, SS-316L showed a much steeper potential drop compared to CuNi30. The electrochemical potential for CuNi30 showed a stable value during the tribocorrosion testing whereas in case of SS-316L, the counter body caused excessive wear loss, resulting in an unstable potential value throughout the test. After the sliding of Al_2O_3 ball was stopped, the potential returned to the initial OCP value. The rate of potential increase in case of SS-316L was slow as compared to CuNi30 because of the difference in passive film formation kinetics for the two alloys.

3.3.2. Potentiodynamic polarization test

In order to access the electrochemical properties under static and sliding conditions, potentiodynamic polarization was studied for both materials. The polarization curves for CuNi30(AB), CuNi30(HT) & SS-316L under static and dynamic conditions are presented in Fig. 11. In the static conditions, CuNi30 showed lower anodic current density values than SS-316L indicating greater corrosion resistance in artificial

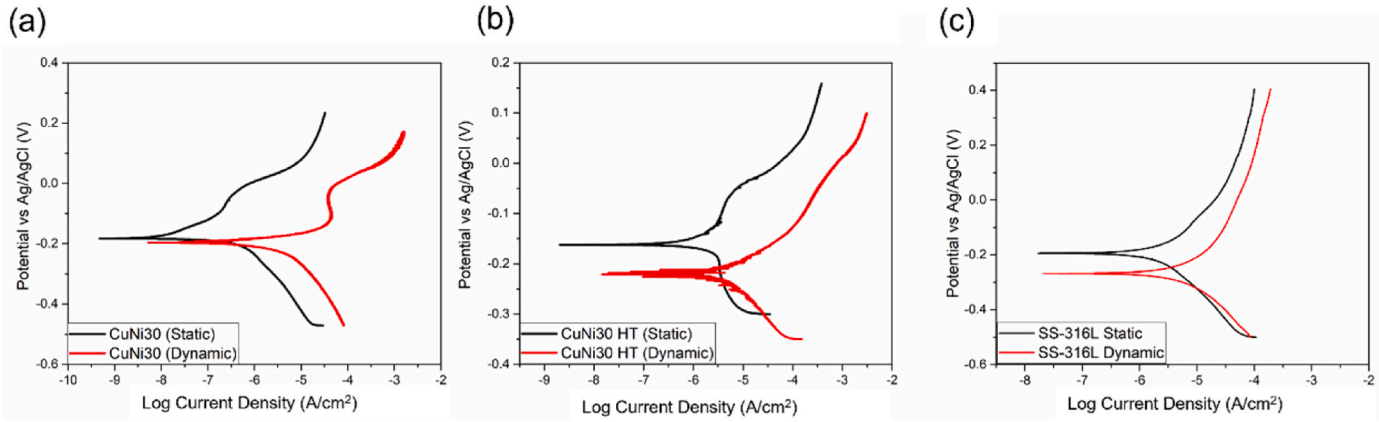

Fig. 11. Polarization curves of CuNi30 (AB), CuNi30(HT) and SS-316L under steady and sliding conditions reveal an increase in corrosion rate in sliding conditions.

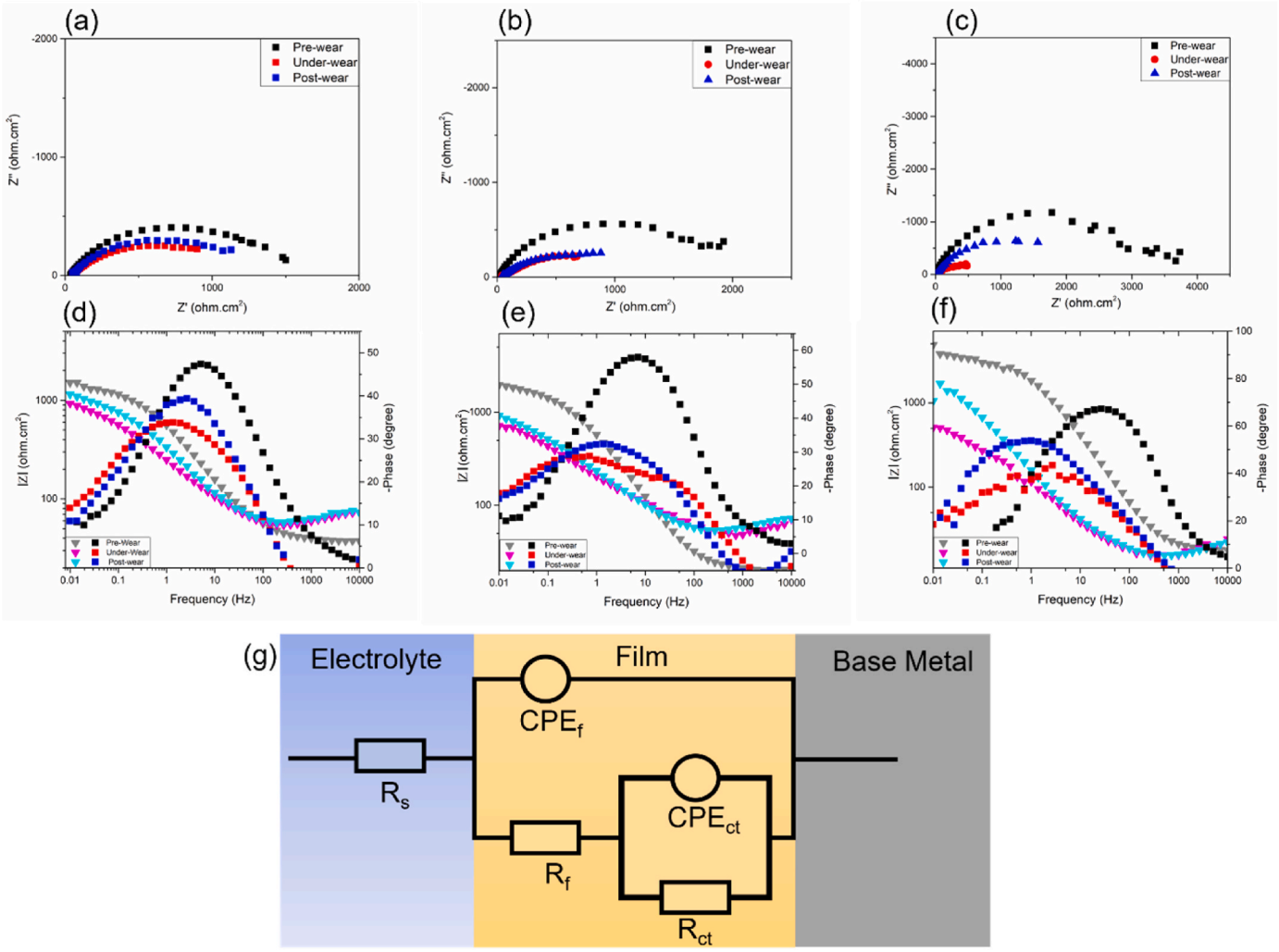

Fig. 12. EIS results (a) (d) for CuNi30 AB, (b) (e) for CuNi30 HT, (c) (f) for SS-316L and (g) equivalent circuit.

seawater. Whereas under sliding conditions, both materials showed a negative shift in self-corrosion potential along with an increase in the anodic response of polarization curve indicating that wear accelerates corrosion. The corrosion potential drop was largest for SS-316L (Static: 0.194V Dynamic: 0.267V) whereas CuNi30 in as-built condition showed the smallest shift in corrosion potential (Static: 0.181V, Dynamic: 0.197V). Furthermore, the anodic current densities under sliding conditions for all tested samples were approximately one order of magnitude higher than their static counterparts. For CuNi30, the current density increased rapidly upon increasing the potential past passive region, which indicates that at higher anodic potential values, the passive oxide layer on SS-316L is more stable than that on CuNi30 which can affect the overall tribocorrosion response at higher potential. While investigating the tribocorrosion behaviour of conventionally manufactured CuNi30, Wei, W. et al. reported that at an applied potential of 0V anodic, the wear loss increased nearly threefold compared to OCP condition, due to enhanced wear-corrosion synergy [30].

3.3.3. *Electrochemical impedance spectroscopy (EIS)*

EIS was performed for CuNi30(AB), CuNi30(HT) and SS-316L samples before, during and after the tribocorrosion experiment. This sequence was adopted to assess the initial static passive behaviour of samples, the dynamic degradation of passive film during sliding and the post-wear repassivation rate of individual samples. Fig. 12 shows the Nyquist and Bode plots for all samples immersed in artificial seawater solution at room temperature (23 °C). The semicircle diameter of the capacitive loop in the Nyquist plots (Fig. 12(a)) corresponds to the charge transfer resistance at the electrode/electrolyte interface [49]. In all samples, the semicircles diameter decreased during tribocorrosion test indicating reduced resistance to electron flow due to repeated breakdown of passive film. The relative decrease in charge transfer resistance was most pronounced in case of SS-316L, suggesting a higher susceptibility to wear-assisted corrosion compared to CuNi30. On the other hand, the low impedance decreases for CuNi30(AB) sample indicates that CuNi30 has a superior repassivation ability and faster recovery towards the initial impedance value, which could explain its improved tribocorrosion resistance against SS-316L.

The impedance responses for all samples were simulated using an equivalent circuit with two-time constants as shown in Fig. 12. The circuit includes R_s (solution resistance), CPE_{dl} (constant phase angle for double layer), R_{ct} (chare transfer resistance), CPE_p (constant phase element for the passive layer) and R_p (resistance of passive layer). Considering surface inhomogeneities such as roughness and impurities, a constant phase element was used instead of pure capacitor [50]. The electrochemical parameters obtained from EIS plots are shown in Table 5. Under static conditions, the polarization resistance R_p defined as the sum of R_f and R_{ct} was higher for heat treated CuNi30 compared to as-built CuNi30 sample, indicating improved corrosion resistance after heat treatment due to microstructure homogenization and reduced defect density [21]. Furthermore, under sliding conditions, both CPE_{cl} and CPE_p increased due to increase in surface roughness and unstable passive film. Under tribocorrosion condition, SS-316L showed lowest R_p

Table 5
Fitting parameters of EIS results calculated using equivalent circuit shown in Fig. 12(g).

Material	Condition	R_s (Ω)	R_f (Ω.cm^2)	R_{cl} (Ω.cm^2)	CPE_f (Ω^{-1}.cm^{-2}.s^{-n})	n_1	CPE_{cl} (Ω^{-1}.cm^{-2}.s^{-n})	n_2
CuNi30 AB	Pre-wear	12.2	1347	1251	1.40E-04	1.09	1.16E-03	0.7
	Under-wear	18	183	741	5.50E-03	0.7	1.40E-03	0.79
	Post-wear	19.1	567	609	7.50E-03	0.7	1.70E-03	0.74
CuNi30 HT	Pre-wear	6.65	1458	1221	7.63E-03	0.93	1.00E-03	0.7
	Under-wear	16.7	128.7	678	8.70E-03	0.7	1.26E-03	0.77
	Post-wear	16.4	142.2	669	8.30E-03	0.7	1.64E-03	0.71
SS-316L AB	Pre-wear	17.4	2900	1078	1.20E-05	0.84	1.38E-03	0.74
	Under-wear	15.5	176	478	5.30E-03	0.7	1.73E-03	0.7
	Post-wear	16.7	218	1550	1.51E-03	0.73	1.73E-04	1.05

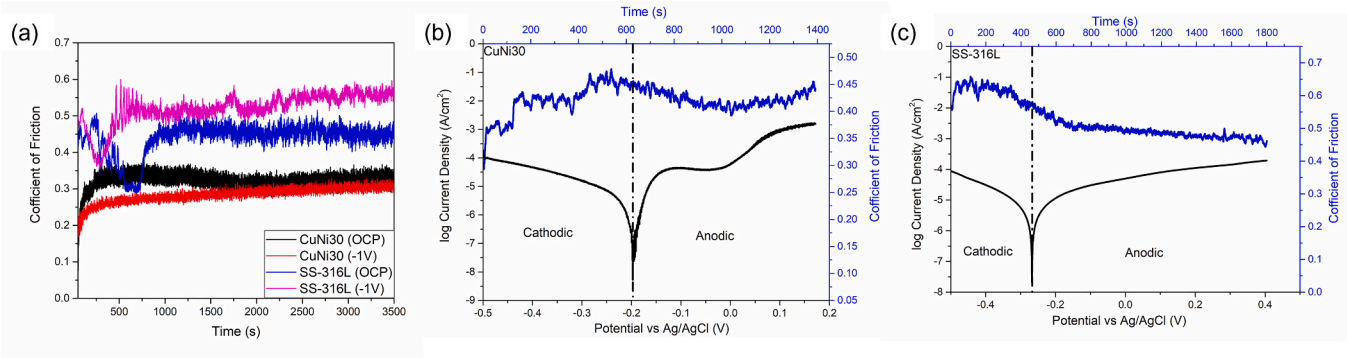

Fig. 13. (a) Average Coefficient of friction for CuNi30 and SS-316L during tribocorrosion test (b) Coefficient of friction during potentiodynamic polarization for CuNi30 and (c) Coefficient of friction during potentiodynamic polarization for SS-316L.

value clearly highlighting its higher susceptibility to tribocorrosion damage. The percentage decrease in R_p values during tribocorrosion revealed that for SS-316L the passive film resistance decreased by 83.5 % compared to CuNi30(AB) which showed a decrease of 65 % from its original value.

3.3.4. Wear behavior

To investigate the wear behaviour, the coefficient of friction (COF) was analysed during cathodic polarization (at -1V), open circuit potential and potentiodynamic polarization (see Fig. 20). Fig. 13(a) shows the evolution of coefficient of friction for CuNi30(AB) and SS-316L alloys at cathodic potential of -1V and under OCP condition. A similar response to CuNi30(AB) was observed for CuNi30(HT) sample, therefore to avoid cluttering its values are not plotted here. The impact of electrochemical corrosion on coefficient of friction is largely governed by the lubricating properties of tribofilm. For SS-316L the low COF values at OCP compared to -1V cathodic indicates that at OCP conditions the corrosion products appeared on the surface provided better lubricating effect. Ma, F. et al. [51] observed similar trend while studying the COF under varying potentials for SS-316L in artificial seawater and reported that at high potentials the metal corrosion rate is faster and the formed tribolayer containing $Mg(OH)_2$ and $CaCO_3$ shears easily providing better lubrication. In case of CuNi30 the difference in COF (-1V vs OCP) was negligible indicating that the electrochemical conditions have minimal influence on friction behaviour as confirmed by the wear track cross-sectional profile and total material loss in tribocorrosion conditions shown in Figs. 14 and 21.

The evolution of COF was simultaneously monitored during the potentiodynamic polarization test under sliding conditions as shown in Fig. 13(b) and (c). The COF data plotted against time in potentiodynamic conditions is divided into two zones (cathodic and anodic zone) as demonstrated by dotted line. For SS-316L, the initially high COF in the cathodic region gradually decreased with the increasing potential and eventually stabilizing in the anodic region. This trend reinforces the lubricating effect of oxide layer and corrosion products under OCP and anodic potentials. Similar observation has been reported by Obadele et al. [52] while studying the tribocorrosion of SS-316L in 3.5 % NaCl solution where they linked the reduction of COF to the development of oxide film and smoothening of wear track. For CuNi30 the COF experienced a gradual rise in the cathodic region peaking before corrosion potential. With increasing potential further in the anodic region, a low COF was detected with the minimum value observed in the passive region due to the development of a stable passive film on sample surface. Zhang, B. et al. [53] while investigating the tribocorrosion behaviour of nickel aluminium bronze in artificial seawater solution reported that the low COF at higher anodic potential is linked to the formation of corrosion pits that can decrease the wear contact area and consequently reduced sliding force.

3.3.5. Wear track morphology

The 3D and cross-sectional morphology of wear track was observed for all samples using optical profilometry and presented in Fig. 14. For CuNi30(AB) & CuNi30(HT) samples the wear track was slightly wider and deeper under OCP condition but the overall difference was negligible indicating small corrosion-wear synergetic effect. For SS-316L the profile depth doubled while the width increased by 14 % under OCP conditions compared to pure mechanical wear (at -1V cathodic potential) representing stronger influence of corrosion assisted wear. The surface roughness of all wear tracks was also measured and reported in Fig. 14(j). SS-316L sample under OCP condition showed four times higher area roughness complementing the high wear rate & profile depth. High resolution SEM images of wear tracks under OCP conditions are reported in Fig. 15. All samples showed wear grooves oriented parallel to the sliding direction, indicative of abrasive wear where hard asperities plough into softer material leading to progressive material removal. For CuNi30 in both AB and HT conditions due to less aggressive corrosion, smooth wear grooves with some lamellar exfoliation at edges was observed indicating delamination damage. Whereas in case of SS-316L the wear track showed the presence of oxide particles and pit holes indicating excessive corrosive damage assisted with some pitting corrosion.

In order to further investigate the subsurface deformation

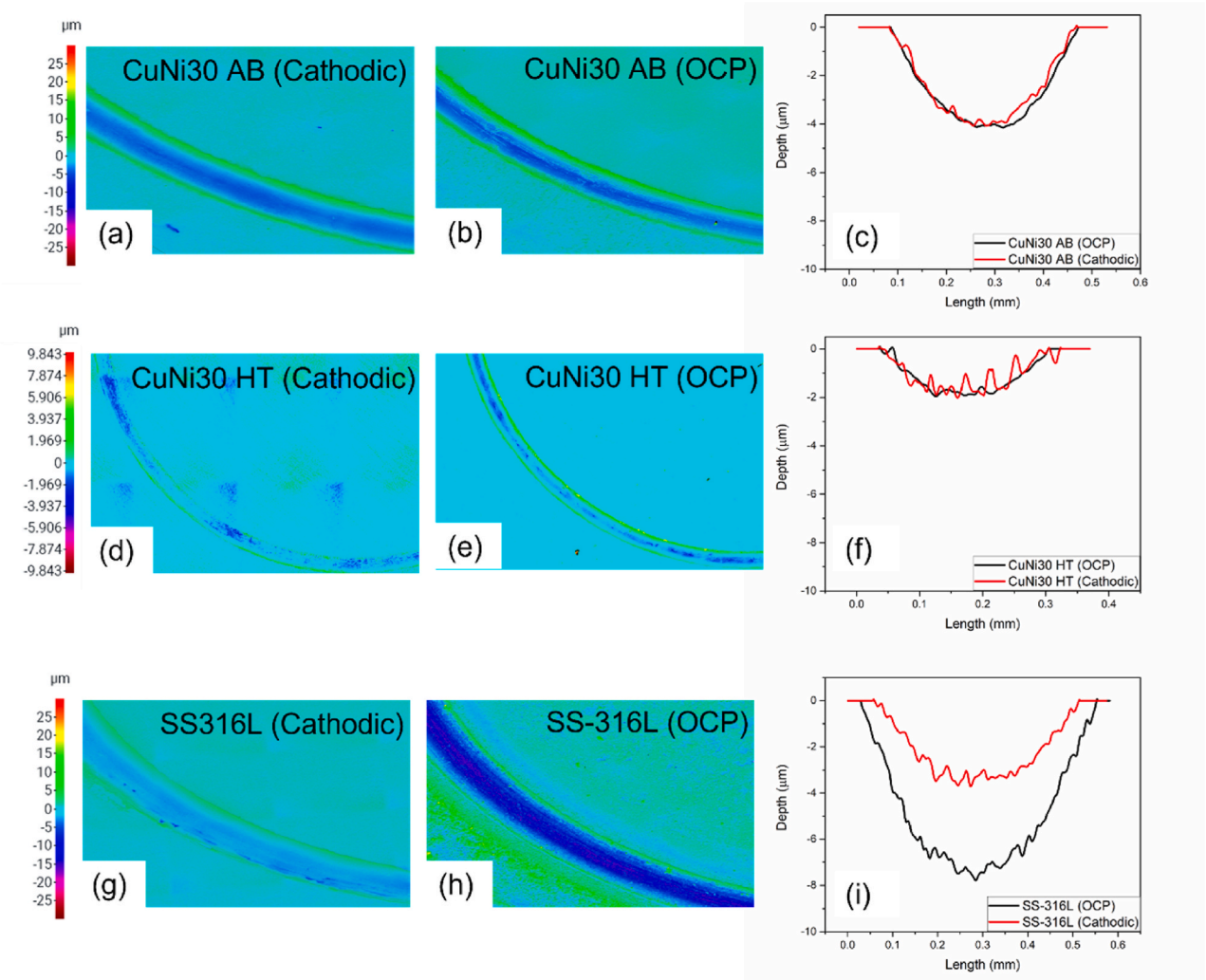

(j)

Material	Condition	Width (mm)	Depth (μm)	Area Roughness Sa (μm)
CuNi30 AB	OCP	0.408± 0.02	4.147± 0.20	0.644± 0.04
	Cathodic	0.389± 0.02	4.069± 0.11	0.528±0.07
CuNi30 HT	OCP	0.270± 0.04	1.825± 0.09	0.194± 0.12
	Cathodic	0.291± 0.07	2.019± 0.10	0.771± 0.08
SS-316L AB	OCP	0.521± 0.06	7.671± 0.12	1.788±0.10
	Cathodic	0.455± 0.03	3.719± 0.08	0.568±0.06

Fig. 14. (a) (,(d) & (g) Comparative 3D morphology at cathodic potential of -1V, (b),(e)&(h) 3D morphology at open circuit potential and (c),(f) & (i) cross-sectional morphology of wear track and (j) calculated wear profile dimensions and roughness.

mechanism, SEM images of FIB cross-sections of the wear track were studied for both CuNi30 and SS-316L as-built samples. SEM images shown in Fig. 16 & Fig. 17 revealed three distinct zones: (1) The bulk material zone with negligible deformation and as-built grain morphology. (2) the middle zone corresponding to the tribologically transformed surface (TTS) which has gone through sever grain refinement due to wear loading. The thickness of TTS region varied between 5 μm and 11 μm for both samples with greater thickness in the middle of track. (3) The top region corresponds to the third body layer (TBL) formed on surface. The estimated thickness of TBL was 217 ± 51 nm for CuNi30 and 71.4 ± 19 nm for SS-316L. The backscatter electron images showed that this top layer is of darker colour indicating that it mostly consists of oxide particles which was further verified through EDS analysis and is presented in Fig. 16(f). The formation of TBL is linked to the mechanical mixing of oxidized surface metal and the underlying TTS zone as reported by Rigney [54] and Guadalupe [55] for Cu/Fe contact and stainless steel alloys. The thickness and stability of TBL plays a key role in enhancing the tribocorrosion resistance by uniformity distributing contact stresses and limiting depassivation through its protective oxide composition [56]. Thus, a thicker TBL layer on CuNi30 further

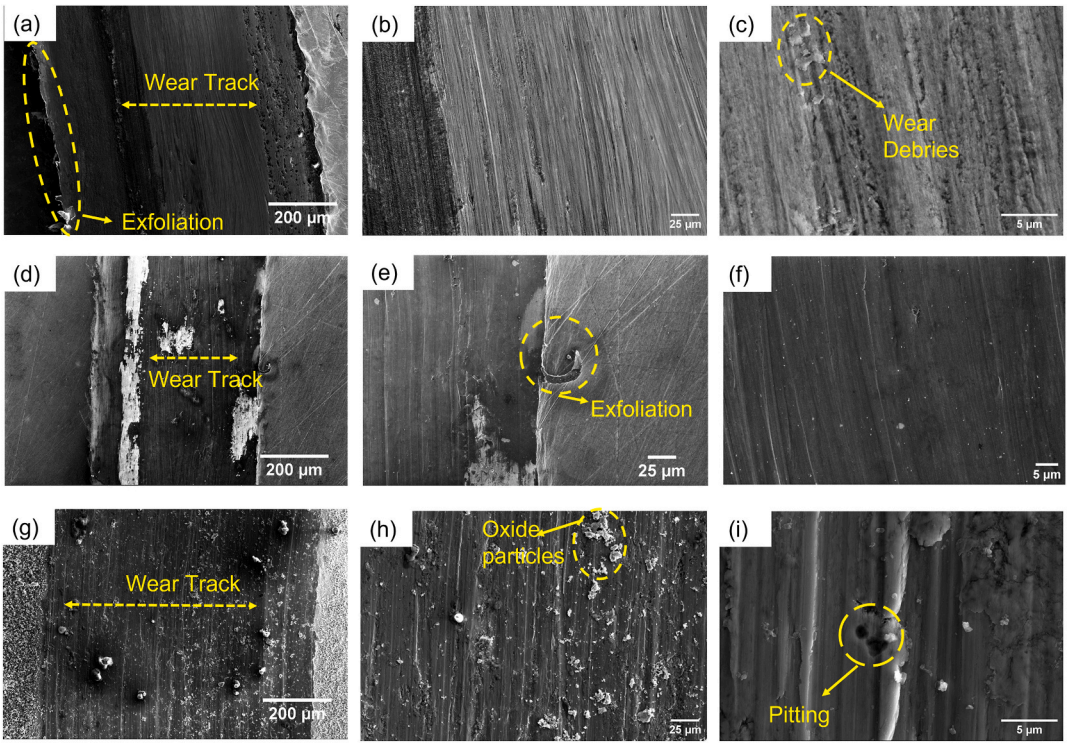

Fig. 15. SEM micrographs at three magnifications showing wear track surface morphology after tribocorrosion in artificial sea water (a), (b) & (c) CuNi30(AB), (d), (e) & (f) CuNi30(HT) and (g), (h) & (i) SS-316L.

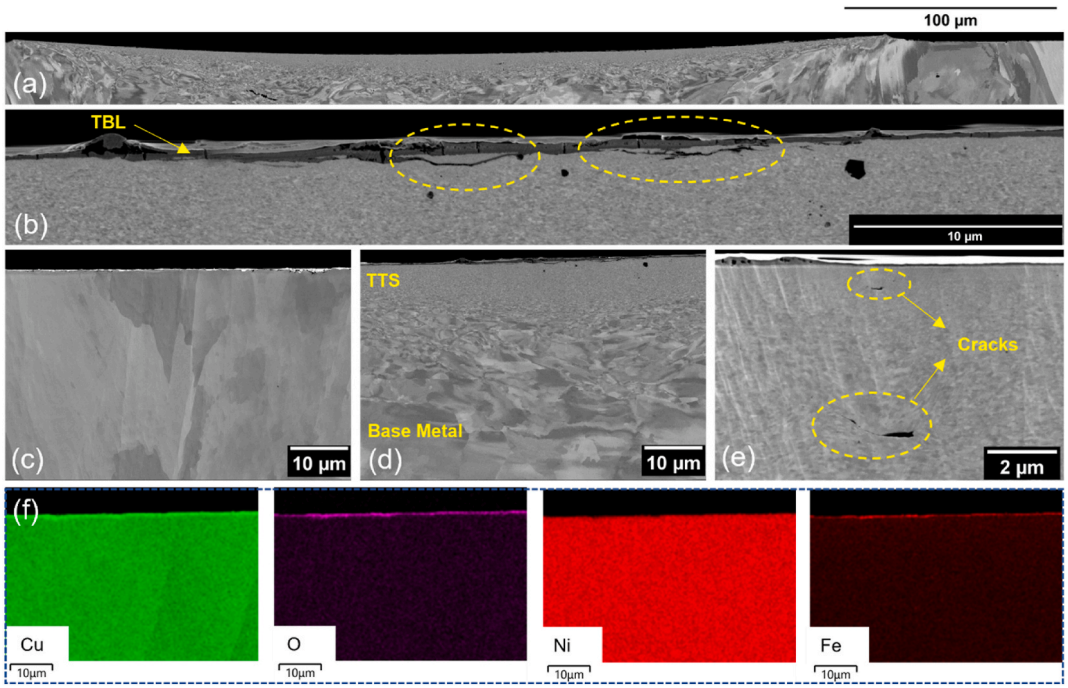

Fig. 16. SEM micrographs showing FIB cross-section for CuNi30 wear track (a) Overview of wear track (b) Third-body layer on top of wear track along with surface cracks (c) as-built region away from track showing course elongated grains (d) Transition from TBL to TTS to Base Metal (e) subsurface cracks generated due to tribocorrosion induced deformation (f) EDS map showing the composition of third body layer.

explains its higher tribocorrosion resistance compared to SS-316L. Several cracks with different sizes and geometry were also identified in the TTS region as shown in Fig. 16(e) which explain the delamination damage of material under tribocorrosion conditions. Wei, W. et al. [30] explained the mechanism of delamination damage while studying the tribocorrosion of conventionally manufactured CuNi30, noting that wear significantly increases subsurface dislocation density, leading to the accumulation of dislocations beneath the contact surface. Over time, these dislocations coalesce to form micro voids, which progressively grow and link to develop subsurface cracks oriented parallel to the

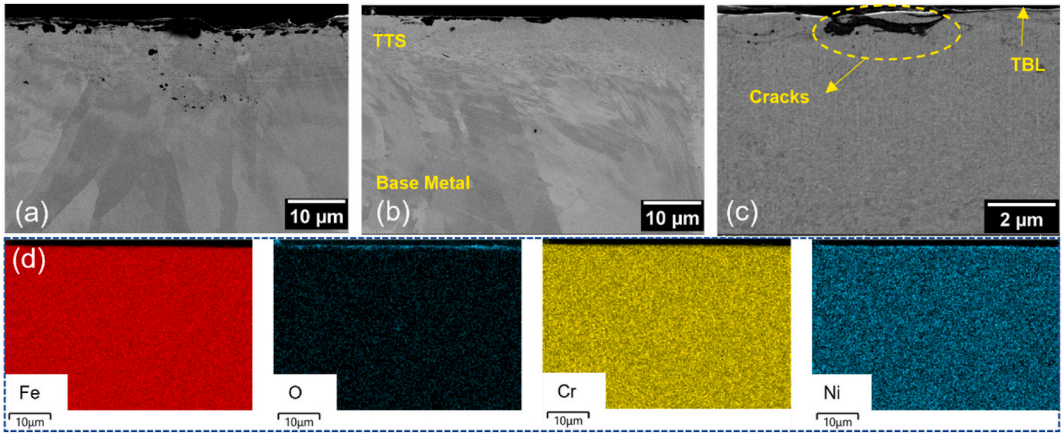

Fig. 17. SEM micrograph showing FIB cross-section for SS-316L (a) as-built region away from wear track (b) Transition from TBL to TTS to Base metal (c) Surface cracks generated as a result of tribocorrosion deformation (d) EDS map highlighting third body layer composition.

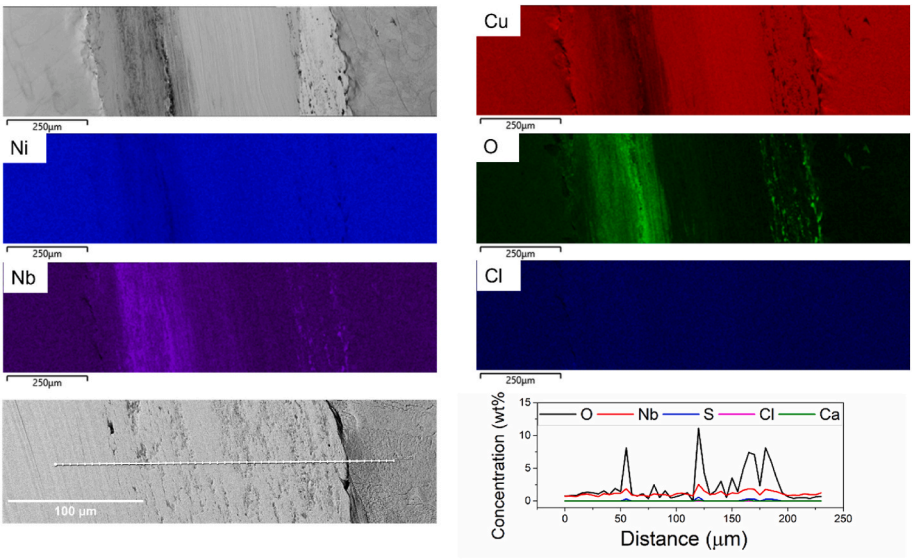

Fig. 18. Surface tribocorrosion morphology, EDS elemental map and line-scan for CuNi30.

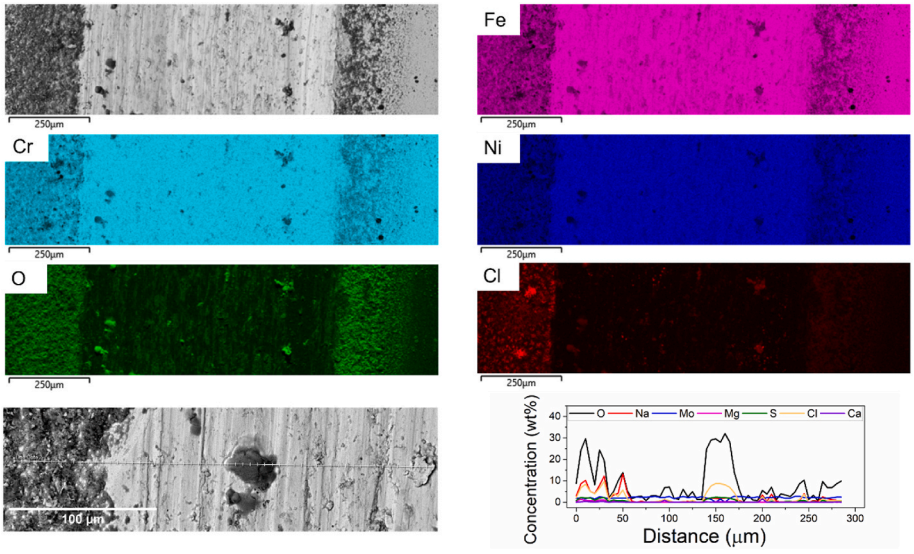

Fig. 19. Surface tribocorrosion morphology, EDS elemental map and line-scan for SS-316L

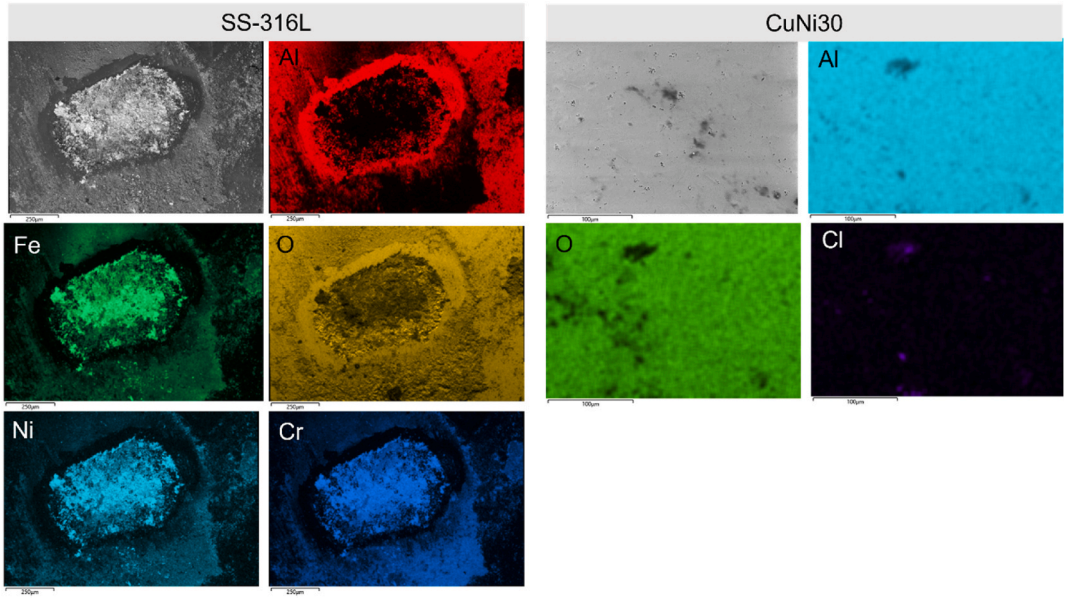

Fig. 20. Surface morphology, EDS elemental map of Alumina counterbody for both CuNi30 and SS-316L samples.

surface. As these cracks propagate and reach a critical size, the surface layers get detached, resulting in the exfoliation of lamellar fragments. Few cracked fragments ready to be detached from surface in subsequent wear are shown in Fig. 16(b).

3.3.6. *Chemical analysis of wear track*

After the completion of tribocorrosion test, EDS study of the wear track was performed. Qualitative data from EDS analysis is given in Figs. 18 and 19 for CuNi30 (AB) and SS316L. The major elements present in the subsequent alloy system as well as in the simulated seawater solution were analysed.

For CuNi30, the elemental map of the wear track showed uniform composition for Cu and Ni indicating the absence of selective corrosion for major alloying elements. However, due to alloy oxidation under tribocorrosion conditions, a significant accumulation of oxides species was observed at the periphery of the wear track. No chlorine enriched particles were observed in the elemental map and line-scan data. The line scan covering the wear track, oxide accumulated area and base sample is also presented in Fig. 18. The maximum oxygen concentration of 11 wt% was observed on the oxide enriched area adjutant to wear track whereas the wear track showed less than 2 wt% oxygen.

In case of SS-316L, no evidence of selective corrosion for the major alloying elements was observed but in addition to the accumulation of oxide particles in the periphery, oxygen rich particles were also observed within the track, indicating excessive oxidation during the process. The average oxygen concentration on the wear track of SS-316L was seven times higher than that observed in CuNi30, supporting the aforementioned electrochemical results, indicating a higher degree of oxidative degradation and corrosion in SS-316L. For SS-316L a significant amount of chlorine was also detected on the wear track suggesting pitting corrosion. Chlorine ions are known to be aggressive in initiating pitting corrosion and their presence in EDS map suggest pitting [57]. In SS-316L the presence of chlorine ions indicates localized breakdown of passive film where the penetration of these chlorine ions acts as a precursor for pitting corrosion [58]. On the contrary CuNi30 sample showed negligible chlorine concentration.

The countersurface Al_2O_3 ball was also investigated using SEM and EDS analysis. Fig. 20 shows the surface morphology and EDS composition maps of Al_2O_3 balls from tests for both materials. No evident signs of abrasion were observed on the alumina ball after tribocorrosion, indicating negligible wear damage to the counter-body. For CuNi30, the contact area of ball did not show elemental presence from CuNi30 alloy suggesting superior tribocorrosion resistance and stable passive film formation. In case of SS-316L a significant amount of corrosion products was also observed attached to the alumina ball indicating severe tribocorrosion response and high degree of mechanical depassivation.

Tribocorrosion is a complex phenomenon resulting from the simultaneous effects of corrosion and mechanical wear. The interplay between these two processes can significantly accelerate the degradation of passive metal alloys during sliding [59]. According to ASTM G-119, the total rate of material loss (T) due to tribocorrosion is give as

$$T = W_o + C_o + S \quad (1)$$

where W_o and C_o represent the material losses due to pure mechanical wear and pure corrosion, respectively, and S accounts for their synergistic effect.

The tribocorrosion synergy can be further divided into two components, the change in corrosion rate due to wear (ΔCw) and the change in wear loss due to corrosion (ΔWc). It is typically expressed as

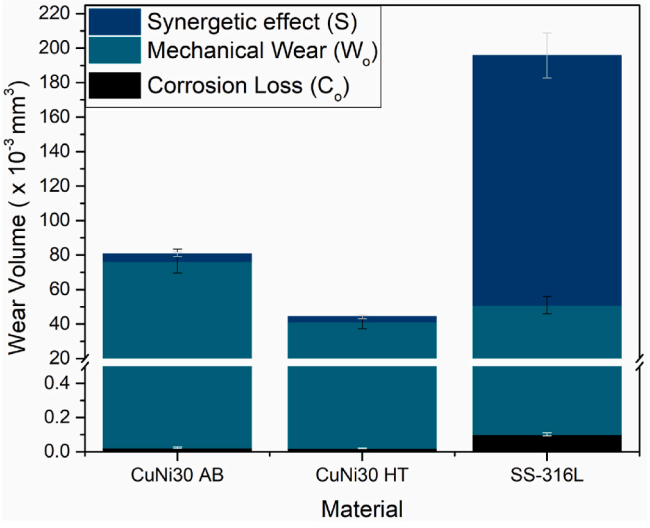

Fig. 21. Total wear track volume of CuNi30 (AB, HT) and SS-316L under mechanical and tribocorrosion conditions in artificial seawater.

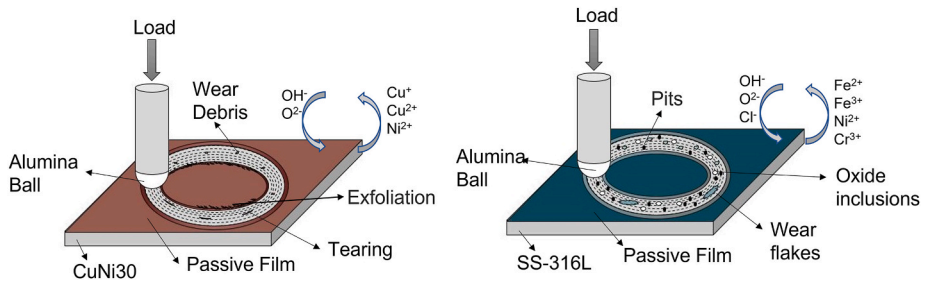

Fig. 22. Schematic diagram showing the effect of artifical seawater on tribocorrosion of (a) CuNi30 and (b) SS-316L

$$S = \Delta Cw + \Delta Wc \tag{2}$$

where

$$\Delta Cw = Cw - Co \tag{3}$$

and

$$\Delta Wc = T - (Wo + Cw) \tag{4}$$

In the above equations, C_w is the corrosion rate in the presence of wear and T is the total material loss in tribocorrosion condition. The total material loss as a result of pure mechanical wear (in artificial seawater at -1V) and in tribocorrosion condition calculated using optical profilometry is presented in Fig. 21 which clearly shows that SS-316L is highly sensitive to synergistic effect as compared to CuNi30. In pure mechanical wear SS-316L showed lower wear volume loss compared to CuNi30 (AB) sample due to high hardness whereas in tribocorrosion condition, the wear volume loss for SS-316L was much higher than CuNi30(AB) and CuNi30(HT) samples. The tribocorrosion wear rate (W) of all samples was calculated using equation (5) where V is the total wear volume, F is the normal load and s is the sliding distance. The calculated wear rates were 3.75×10^{-8} mm^3/N.mm for CuNi30 AB, 2.08×10^{-8} mm^3/N.mm for CuNi30 HT and 9.07×10^{-8} mm^3/N.mm for SS-316L.

$$W = V/F.s \tag{5}$$

The key findings outlined above are visually represented in Fig. 22. Under tribocorrosion conditions, CuNi30 demonstrated superior performance characterized by low potential decrease under dynamic conditions, higher polarization resistance and thick third body layer formation. The coefficient of friction (COF) for CuNi30 remained low and stable (0.28–0.31) under both open circuit potential (OCP) and cathodic conditions (-1V) indicating minimal influences of electrochemical environment on tribocorrosion. The COF data along with the total wear volume highlights CuNi30 robustness and suitability for tribocorrosion applications.

In contrast, SS-316L exhibited significantly lower tribocorrosion resistance. Electrochemical data supported by SEM observations, revealed severe corrosion damage and some localized pitting in SS-316L samples. The pronounced surface degradation was also reflected in the high COF values (0.44–0.55) compared to CuNi30. Moreover, the wear profile of SS-316L under OCP conditions was significantly deeper than that observed under cathodic polarization, underscoring the significant effect of corrosion assisted wear in the degradation of SS-316L surface.

In summary, additively manufactured CuNi30 exhibited an excellent combination of high strength, ductility and superior seawater corrosion resistance. The findings reported here showing the minimal degradation of CuNi30 in tribocorrosion conditions compared to SS-316L, signifies CuNi30 as a promising material for marine structural application. Although the material cost of CuNi30 is quite high compared to SS-316L, but the cost-effectiveness and on-demand manufacturing capabilities of PBF-LB/M makes additively manufactured CuNi30 a compelling choice for enhanced durability and efficiency of marine structures.

4. Conclusion

This study investigated the mechanical properties and tribocorrosion behaviour of additively manufactured CuNi30 and SS-316L processed via PBF-LB/M for marine applications. Based on the experimental results, the following conclusions are drawn.

1. Under optimal processing conditions, additively manufactured CuNi30 achieved a high relative density of 99.7 %, indicating excellent printability via PBF-LB/M and demonstrating PBF-LB/M suitability for manufacturing small size CuNi30 structural components for marine industry.
2. Heat treatment at 550 °C for 2 h significantly improved the hardness and tensile strength of CuNi30, making it comparable to SS-316L where Nb rich precipitation ($NbNi_3$) contributed to strengthening through precipitation hardening.
3. The electrochemical measurements showed a higher polarization resistance decrease for SS-316L compared to CuNi30 under tribocorrosion conditions suggesting greater susceptibility of SS-316L to tribocorrosion damage.
4. For CuNi30, comparable material loss and consistent COF values under both cathodic (-1V) and OCP conditions and the formation of a thicker third body layer during tribocorrosion indicates low susceptibility to wear-corrosion synergetic effect, thus highlighting materials ability to maintain superior tribological performance under electrochemical conditions.
5. Compared to SS-316L, the as-built and heat-treated CuNi30 showed 59 % and 77 % lower wear rates, respectively, indicating a substantial improvement in tribocorrosion resistance.

Declaration of competing interest

The authors declare that they have no known competing financial interests or personal relationships that could have appeared to influence the work reported in this paper.

Acknowledgment

We sincerely thank Aki Piiroinen for his invaluable assistance with various laboratory activities at DMS, UTU. Our gratitude also goes to Frej Björndahl (FNT, Abo Academy) for conducting the particle size distribution analysis and Anssi Peuronen (IMC, UTU) for helping with the XRD measurements. The authors also gratefully acknowledge the financial support provided by Neles Oy Foundation and AIMM project funded by FICORE network (University of Turku Seed Funding). Prof. Ashish Ganvir acknowledges financial support from GREEN-BAT (352517), co-funded by the Research Council of Finland and the European Union under the M-ERA.NET 2021 framework, as well as the SOLACE (DNR 360540) Academy research fellowship, funded by the Research Council of Finland. He also extends his gratitude to the City of Turku for supporting his tenure-track grant. Prof. Antti Salminen acknowledges financial support through the DREAMS TENK TOT project (5159/31/2021), funded by Business Finland.

Appendix A. Supplementary data

Supplementary data to this article can be found online at https://doi.org/10.1016/j.jmrt.2025.10.247.

References

[1] Lee M, Kim B, Kwon Y, Kim J. Characteristics of the marine environment and algal blooms in Gamak Bay. Fish Sci Apr. 2009;75(2):401–11. https://doi.org/10.1007/s12562-009-0056-6.

[2] Xu L, Xin Y, Ma L, Zhang H, Lin Z, Li X. Challenges and solutions of cathodic protection for marine ships. Corros Commun Jun. 2021;2:33–40. https://doi.org/10.1016/j.corcom.2021.08.003.

[3] Cheng J, Wang Z, Gan X, Lei Q, Li Z, Zhou K. Corrosion and corrosive-wear behaviors of a high strength and toughness Cu–15Ni–8Sn alloy in seawater. Mater Corros 2020;71(4):593–607. https://doi.org/10.1002/maco.201911323.

[4] Lingwall BA, Sexton TN, Cooley CH. Polycrystalline diamond bearing testing for marine hydrokinetic application. Wear Apr. 2013;302(1):1514–9. https://doi.org/10.1016/j.wear.2012.11.068.

[5] Yuan SJ, Pehkonen SO. Surface characterization and corrosion behavior of 70/30 Cu–Ni alloy in pristine and sulfide-containing simulated seawater. Corros Sci Mar. 2007;49(3):1276–304. https://doi.org/10.1016/j.corsci.2006.07.003.

[6] North RF, Pryor MJ. The influence of corrosion product structure on the corrosion rate of Cu-Ni alloys. Corros Sci Jan. 1970;10(5):297–311. https://doi.org/10.1016/S0010-938X(70)80022-1.

[7] Gao S, Zhang M, Ding J, He X, Chen H, Zhou S. Tailoring the microstructure and mechanical properties for additive manufactured CuNi30 alloy via in-situ NbC formation. Mater Lett Sep. 2025;395:138714. https://doi.org/10.1016/j.matlet.2025.138714.

[8] Kreil A, Vosskühler H, Walter K. The continuous casting of copper and its alloys. Metall Rev Jan. 1960;5(1):413–46. https://doi.org/10.1179/mtlr.1960.5.1.413.

[9] Bhattacharya S, Dinda GP, Dasgupta AK, Natu H, Dutta B, Mazumder J. Microstructural evolution and mechanical, and corrosion property evaluation of Cu–30Ni alloy formed by direct metal deposition process. J Alloys Compd Jun. 2011;509(22):6364–73. https://doi.org/10.1016/j.jallcom.2011.03.091.

[10] Deyong L, Elboujdani M, Tremblay R, Ghali E. Electrochemical behaviour of rapidly solidified and conventionally cast Cu-Ni-Sn alloys. J Appl Electrochem Sep. 1990;20(5):756–62. https://doi.org/10.1007/BF01094302.

[11] Hu Z, Nie X, Qi Y, Zhang H, Zhu H. Cracking criterion for high strength Al–Cu alloys fabricated by selective laser melting. Addit Manuf Jan. 2021;37:101709. https://doi.org/10.1016/j.addma.2020.101709.

[12] Rankouhi B, Jahani S, Pfefferkorn FE, Thoma DJ. Compositional grading of a 316L-Cu multi-material part using machine learning for the determination of selective laser melting process parameters. Addit Manuf Feb. 2021;38:101836. https://doi.org/10.1016/j.addma.2021.101836.

[13] Ye X, Miao X, Shi X, Wu M. Influence of volumetric energy density on microstructure evolution and tribo-corrosion properties of LPBF-fabricated Ti–4Cu alloy. Met Mater Int Jul. 2024;30(7):2023–37. https://doi.org/10.1007/s12540-023-01615-3.

[14] Wang J, Zhou XL, Li J, Brochu M, Zhao YF. Microstructures and properties of SLM-Manufactured Cu-15Ni-8Sn alloy. Addit Manuf Jan. 2020;31:100921. https://doi.org/10.1016/j.addma.2019.100921.

[15] Cook PS, Murphy AB. Simulation of melt pool behaviour during additive manufacturing: underlying physics and progress. Addit Manuf Jan. 2020;31:100909. https://doi.org/10.1016/j.addma.2019.100909.

[16] Sabzi HE, et al. Grain refinement in laser powder bed fusion: the influence of dynamic recrystallization and recovery. Mater Des Nov. 2020;196:109181. https://doi.org/10.1016/j.matdes.2020.109181.

[17] Wallis C, Buchmayr B. Effect of heat treatments on microstructure and properties of CuCrZr produced by laser-powder bed fusion. Mater Sci Eng, A Jan. 2019;744:215–23. https://doi.org/10.1016/j.msea.2018.12.017.

[18] Bonesso M, et al. Analysis and development of cucrzr alloy fabrication in lpbf: impact of process parameters and heat treatments on thermo-mechanical properties. Rochester, NY: Social Science Research Network; Nov. 18, 2024, 5025000. https://doi.org/10.2139/ssrn.5025000.

[19] Nadimi M, Song J, Cheng L, Fu Y. Corrosion evaluation and microstructural characteristics of 70/30 copper-nickel alloy fabricated by laser powder bed fusion. J Alloys Metall Syst Mar. 2025;9:100155. https://doi.org/10.1016/j.jalmes.2025.100155.

[20] Liu Z, et al. Investigation on mechanical properties and corrosion behavior of laser powder bed fusion 70/30 copper-nickel alloy. Corros Sci May 2024;232:112040. https://doi.org/10.1016/j.corsci.2024.112040.

[21] Roshan M, et al. Powder bed fused–laser beam (PBF-LB) 70/30 copper-nickel (Cu-30Ni): hierarchical microstructure and mechanical properties. J Alloys Compd Sep. 2025;1039:183312. https://doi.org/10.1016/j.jallcom.2025.183312.

[22] Ponthiaux P, Wenger F, Drees D, Celis JP. Electrochemical techniques for studying tribocorrosion processes. Wear Mar. 2004;256(5):459–68. https://doi.org/10.1016/S0043-1648(03)00556-8.

[23] Salasi M, Stachowiak GB, Stachowiak GW. New experimental rig to investigate abrasive–corrosive characteristics of metals in aqueous media. Tribol Lett Oct. 2010;40(1):71–84. https://doi.org/10.1007/s11249-010-9640-2.

[24] Wood RJK, Lu P. Coatings and surface modification of alloys for tribo-corrosion applications. Coatings Jan. 2024;14(1):1. https://doi.org/10.3390/coatings14010099.

[25] Zhu Y, Liu H, Zhang D, Wang J, Yan F. Effect of polarization potentials on tribocorrosion behavior of Monel 400 alloy in seawater environment. Tribol Int Apr. 2022;168:107445. https://doi.org/10.1016/j.triboint.2022.107445.

[26] Watson SW, Friedersdorf FJ, Madsen BW, Cramer SD. Methods of measuring wear-corrosion synergism. Wear Mar. 1995;181–183:476–84. https://doi.org/10.1016/0043-1648(95)90161-2.

[27] Assi F, Böhni H. Study of wear–corrosion synergy with a new microelectrochemical technique1. Wear Dec. 1999;233–235:505–14. https://doi.org/10.1016/S0043-1648(99)00237-9.

[28] Chen J, Zhang Q, Li Q, Fu S, Wang J. Corrosion and tribocorrosion behaviors of AISI 316 stainless steel and Ti6Al4V alloys in artificial seawater. Trans Nonferrous Metals Soc China Apr. 2014;24(4):1022–31. https://doi.org/10.1016/S1003-6326(14)63157-5.

[29] Tan L, Wang Z, Ma Y. Tribocorrosion behavior and degradation mechanism of 316L stainless steel in typical corrosive media. Acta Metall Sin Engl Lett Jun. 2021;34(6):813–24. https://doi.org/10.1007/s40195-020-01182-1.

[30] Wei W, Liu C, Xie H, Gong B, Gong K, Mao F. Effect of polarization potential on the tribocorrosion behavior of 70/30 Cu-Ni alloy. J Mater Eng Perform Jun. 2024. https://doi.org/10.1007/s11665-024-09631-z.

[31] Stachowiak A, Wieczorek D, Gruber K, Bartkowski D, Bartkowska A, Ulbrich D. Comparison of tribocorrosion resistance of inconel® 718 alloy manufactured by conventional method and laser powder bed fusion method. Tribol Int Apr. 2023;182:108368. https://doi.org/10.1016/j.triboint.2023.108368.

[32] B369 standard specification for copper-nickel alloy castings. Accessed: Feb. 17, 2025. [Online]. Available: https://www.astm.org/b0369-09.html.

[33] ASTM International. Standard specification for stainless steel bars and shapes. ASTM A276. ASTM International; 2021.

[34] Gopaluni A, Nayak C, Piironen A, Kantonen T, Salminen A. Effects of powder recycling on laser-based powder bed fusion produced SS316L parts. IOP Conf Ser Mater Sci Eng Dec. 2023;1296(1):012021. https://doi.org/10.1088/1757-899X/1296/1/012021.

[35] ASTM International. Standard test methods for tension testing of metallic materials. West Conshohocken, PA: ASTM; 2021. E8/E8M-21.

[36] Standard practice for preparation of substitute ocean water. Accessed: Dec. 17, 2024. [Online]. Available: https://www.astm.org/d1141-98r21.html.

[37] Möller H, Boshoff ET, Froneman H. The corrosion behaviour of a low carbon steel in natural and synthetic seawaters. J South Afr Inst Min Metall Aug. 2006;106:585–92.

[38] Microstructure, precipitates and mechanical properties of powder bed fused inconel 718 before and after heat treatment. Accessed: Jul. 07, 2025. [Online]. Available: https://www.jmst.org/article/2019/1005-0302/1005-0302-35-6-1153.shtml?utm_source=chatgpt.com.

[39] Sanchez S, et al. Powder bed fusion of nickel-based superalloys: a review. Int J Mach Tool Manufact Apr. 2021;165:103729. https://doi.org/10.1016/j.ijmachtools.2021.103729.

[40] Diaz Vallejo N, Lucas C, Ayers N, Graydon K, Hyer H, Sohn Y. Process optimization and microstructure analysis to understand laser powder bed fusion of 316L stainless steel. Metals May 2021;11(5):5. https://doi.org/10.3390/met11050832.

[41] Behjat A, Shamanian M, Iuliano L, Saboori A. Laser powder bed fusion in situ alloying of AISI 316L-2.5%Cu alloy: microstructure and mechanical properties evolution. Prog Addit Manuf Jan. 2024. https://doi.org/10.1007/s40964-023-00557-x.

[42] Saboori A, Piscopo G, Lai M, Salmi A, Biamino S. An investigation on the effect of deposition pattern on the microstructure, mechanical properties and residual stress of 316L produced by directed energy deposition. Mater Sci Eng, A Apr. 2020;780:139179. https://doi.org/10.1016/j.msea.2020.139179.

[43] Raffeis I, et al. Qualification of a Ni–Cu alloy for the laser powder bed fusion process (LPBF): its microstructure and mechanical properties. Appl Sci Jan. 2020;10(10):10. https://doi.org/10.3390/app10103401.

[44] Avila-Salgado DA, Juárez-Hernández A, Medina-Ortíz F, Banda ML, Hernández-Rodríguez MAL. Influence of B and Nb Additions and Heat Treatments on the Mechanical Properties of Cu-Ni-Co-Cr-Si Alloy for High Pressure Die Casting Applications. Metals May 2020;10(5):602. https://doi.org/10.3390/met10050602.

[45] Raghavan M. Precipitation in a Cu-30 Pct Ni-1 Pct Nb alloy. Metall Trans A Jul. 1977;8(7):1071–8. https://doi.org/10.1007/BF02667392.

[46] Nan J, Xiao Q, Yao D, Wang J. Effect of normal load and strain accumulation on tribological properties of Al3003/St12 multilayered composite produce by severe plastic deformation. Arch Civ Mech Eng Jan. 2025;25(1):1–18. https://doi.org/10.1007/s43452-024-01105-2.

[47] Ishikawa K. Fractals in dimple patterns of ductile fracture. J Mater Sci Lett Apr. 1990;9(4):400–2. https://doi.org/10.1007/BF00721011.

[48] Ikeshoji T, Suzumura A. 320 fractal dimension of ductile fractured surface and the dimple size distribution. Proc JSME Mater Process Conf MP 2002;10(1):580–5. https://doi.org/10.1299/jsmeintmp.10.1.580.

[49] Metikoš-Huković M, Babić R, Škugor I, Grubač Z. Copper–nickel alloys modified with thin surface films: corrosion behaviour in the presence of chloride ions. Corros Sci Jan. 2011;53(1):347–52. https://doi.org/10.1016/j.corsci.2010.09.041.

[50] Nadimi M, Song J, Cheng L, Fu Y. Corrosion evaluation and microstructural characteristics of 70/30 copper-nickel alloy fabricated by laser powder bed fusion. Rochester, NY: Social Science Research Network; Sep. 25, 2024, 4967915. https://doi.org/10.2139/ssrn.4967915.

[51] Ma F, Li J, Zeng Z, Gao Y. Tribocorrosion behaviour of F690 and 316L steel in artificial seawater. Lubric Sci 2018;30(7):365–75. https://doi.org/10.1002/ls.1427.

[52] Obadele BA, Andrews A, Shongwe MB, Olubambi PA. Tribocorrosion behaviours of AISI 310 and AISI 316 austenitic stainless steels in 3.5% NaCl solution. Mater Chem Phys Mar. 2016;171:239–46. https://doi.org/10.1016/j.matchemphys.2016.01.013.

[53] Zhang B, Wang J, Yan F. Load-dependent tribocorrosion behaviour of nickel-aluminium bronze in artificial seawater. Corros Sci Feb. 2018;131:252–63. https://doi.org/10.1016/j.corsci.2017.11.028.

[54] Rigney DA, Karthikeyan S. The evolution of tribomaterial during sliding: a brief introduction. Tribol Lett Jul. 2010;39(1):3–7. https://doi.org/10.1007/s11249-009-9498-3.

[55] Guadalupe S, Falcand C, Chitty W, Mischler S. Tribocorrosion in pressurized high-temperature water: a mass flow model based on the third-body approach. Tribol Lett Mar. 2016;62(1):10. https://doi.org/10.1007/s11249-016-0653-3.

[56] Dalmau A, Muñoz AI, Mischler S. Current and friction transients during tribocorrosion of a biomedical titanium alloy sliding against zirconia. Wear Jul. 2023;524–525:204821. https://doi.org/10.1016/j.wear.2023.204821.

[57] Gnanavelbabu A, Amul XJ, Surendran KTS. Investigation on the tribocorrosion and electrochemical corrosion behaviour of AA2014/Al2O3 nanocomposites fabricated through ultrasonication coupled stir-squeeze casting method. J Appl Electrochem Apr. 2022;52(4):765–91. https://doi.org/10.1007/s10800-022-01666-1.

[58] Gudić S, Vrsalović L, Matošin A, Krolo J, Oguzie EE, Nagode A. Corrosion behavior of stainless steel in seawater in the presence of sulfide. Appl Sci Jan. 2023;13(7):7. https://doi.org/10.3390/app13074366.

[59] Hameed Abdulmajeed M, Anaee R. Tribocorrosion. 2016. p. 89–110.